Topological Atomic Spin Wave Lattices by Dissipative Couplings

Dongdong Hao,[1] Lin Wang,[1] Xingda Lu,[1] Xuzhen Cao,[2,3] Suotang Jia,[2,3] Ying Hu,[2,3,*] and Yanhong Xiao[2,3,1,†]
[1]Department of Physics, State Key Laboratory of Surface Physics and Key Laboratory of Micro and Nano Photonic Structures (Ministry of Education), Fudan University, Shanghai 200433, China
[2]State Key Laboratory of Quantum Optics and Quantum Optics Devices, Institute of Laser Spectroscopy, Shanxi University, Taiyuan 030006, China
[3]Collaborative Innovation Center of Extreme Optics, Shanxi University, Taiyuan 030006, China

(Received 27 March 2022; revised 15 January 2023; accepted 27 February 2023; published 12 April 2023)

Recent experimental advances in creating dissipative couplings provide a new route for engineering exotic lattice systems and exploring topological dissipation. Using the spatial lattice of atomic spin waves in a vacuum vapor cell, where purely dissipative couplings arise from diffusion of atoms, we experimentally realize a dissipative version of the Su-Schrieffer-Heeger (SSH) model. We construct the dissipation spectrum of the topological or trivial lattices via electromagnetically induced-transparency spectroscopy. The topological dissipation spectrum is found to exhibit edge modes within a dissipative gap. We validate chiral symmetry of the dissipative SSH couplings and also probe topological features of the generalized dissipative SSH model. This work paves the way for realizing non-Hermitian topological quantum optics via dissipative couplings.

DOI: 10.1103/PhysRevLett.130.153602

Introduction.—Topological phases of quantum matter host fascinating phenomena, such as edge modes that are immune to imperfections [1–4], with potential applications in quantum computation and other technologies [5–7]. The robust nature of these phenomena in wide classes of lattice systems is linked to the presence of energy gaps and topologically nontrivial energy bands in the bulk; this protects edge modes, at energies within the bulk energy gap, from symmetry-preserving local perturbations.

Recently, dissipative couplings have been realized in various settings, such as atoms [8], heat transfer systems [9], circuits [10], optomechanical systems [11], waveguides [12], resonators [13], and laser arrays [14], etc. These advances opened up novel possibilities for designing topological structures [15–22]. Lattice systems with purely dissipative couplings exhibit distinct spectral features from the coherently coupled networks in a Hamiltonian context and may enable topological dissipation; i.e., topological properties are associated with the gapped damping bands (or bands of dissipation rates) in the bulk and dissipative edge modes within the dissipative gap, decoupled from the bulk. These intriguing phenomena, however, remain largely unexplored experimentally, with only a recent implementation using synthetic dimensions of photonic resonator with time-multiplexed pulses [23].

Atomic vapor systems offer a unique platform for exploring topological dissipation. Such systems involve a non-Markovian reservoir, where rapid transport of atomic coherence via atomic diffusions [24] naturally leads to dissipative coupling between long-lived atomic spin waves created by electromagnetically induced transparency (EIT) [25] in spatially separated optical channels. This can mediate quantum optical spatial correlations as recently observed [26,27]. Realizing topological dissipation therein may promise topology-enabled quantum correlations and non-Hermitian topological quantum optics, complementary to topological quantum optics based on conservative couplings [28–30].

Here we experimentally realize the dissipative version of the paradigmatic Su-Schrieffer-Heeger (SSH) model, based on a spatial lattice of atomic spin waves in a vacuum vapor cell. Utility of the vacuum cell (i.e., no wall coatings [31]) allows us to realize the nearest-neighbor dissipative couplings, hard to achieve in the wall-coated cell in previous experiments [8] due to the all-to-all couplings therein. We control the coupling rates via the spacing between optical beams, thus inducing topological or trivial dissipation. By constructing the dissipation spectra via EIT spectroscopy, we show the topological dissipation spectrum exhibits edge modes at zero dissipation rates (relative to the background loss) within a bulk dissipative gap. We also create a ring pattern simulating a dissipative SSH model with periodic boundaries and spectroscopically validate its chiral symmetry. Finally, we observe the weakly dissipative edge modes featured in the dissipative version of the generalized SSH model [32]. Our experiments agree well with the theoretical analysis.

Dissipatively coupled SSH array by flying atoms.—Our experiments utilize an enriched ^{87}Rb vacuum vapor cell [Fig. 1(a)] with no buffer gas or wall coating of cylindrical shape with a diameter of 2.5 cm and length 5 cm, and housed within a three-layer magnetic shield to screen out

 © 2023 American Physical Society

ambient magnetic fields. The cell temperature is set to 40 °C to maintain a relatively small optical depth. The output of a diode laser, tuned to the Rb D1 transition $5S_{1/2}F = 2 \rightarrow 5P_{1/2}F' = 1$, passes through a polarization-maintaining optical fiber and is then divided into several spatially separated beams, forming optical channels in the cell. Each channel is composed of a right-circularly polarized strong control field (Rabi frequency Ω_c) and a left-circularly polarized weak probe (Ω_p) forming a standard Λ-type EIT configuration with ground states $|1\rangle$,$|2\rangle$ and excited state $|3\rangle$, which creates a local atomic spin wave (i.e., ground-state coherence ρ_{12}). A uniform magnetic field is applied to induce Zeeman shifts to the energy levels for the adjustment of two-photon detuning δ_B. Spin waves in different optical channels are dissipatively coupled through atomic motion. The coupling rate is controlled through the channel separation d with a $1/d$ scaling (see Supplemental Material [33]), while the laser beam diameter is set to 1.5 mm for all the beams. When channels are aligned in a straight line, the direct atom-flight path (for the ground-state coherence) between the beyond-nearest-neighbor channels is largely "blocked" via optical pumping of the channel(s) in between, and we effectively realize nearest-neighbor couplings. Thus, by patterning $2N$ channels with alternating spacings d_1 and d_2, we synthesize a dissipative form of the SSH model, with lattice site j represented by the ground-state coherence $\rho_{12}^{(j)}$ in channel j ($j = 1, \ldots, 2N$).

According to the standard density matrix formalism [33], our system can be described by the equation of motion $\partial_t \boldsymbol{\rho}_{12} = -i[(\delta_B - i\gamma)I + H]\boldsymbol{\rho}_{12} + \mathbf{P}_{\text{in}}$. Here, the vector $\boldsymbol{\rho}_{12} \equiv [\rho_{12}^{(1)}, \ldots, \rho_{12}^{(2N)}]^T$ denotes the ground-state coherence distribution across the channels, I is a unity matrix, γ is the dephasing rate dominated by the transit broadening common to all channels, and the vector $\mathbf{P}_{\text{in}} \equiv [P_{\text{in}}^{(1)}, \ldots, P_{\text{in}}^{(2N)}]^T$ denotes the pumping sources of the coherence by the input light fields, where $\mathrm{P}_{\text{in}}^{(j)} = -\Omega_c^{(j)*}\Omega_p^{(j)}/\gamma_{23}$ with γ_{23} as the optical coherence decay rate. The non-Hermitian SSH Hamiltonian H reads

$$H = ive^{i\delta_B d_1/v}\sum_m (|a,m\rangle\langle b,m| + |b,m\rangle\langle a,m|) + iwe^{i\delta_B d_2/v}\sum_m (|b,m\rangle\langle a,m+1| + |a,m+1\rangle\langle b,m|), \quad (1)$$

where $|a,m\rangle$ ($|b,m\rangle$) denotes $\rho_{12}^{(j)}$ in odd $j = 2m-1$ (even $j = 2m$) numbered channels in unit cell $m = 1, \ldots, N$. The intra- and intercell dissipative coupling rates v and w satisfy $v/w \propto d_2/d_1$. A relative phase $\delta_B(d_2 - d_1)/v$ between the intra- and intercell couplings accumulates during the atomic flow (at velocity v) between neighboring beams and is the same in either direction.

The non-Hermitian Hamiltonian H reduces to H_0 when $\delta_B = 0$, realizing a purely dissipative version of the paradigmatic SSH model. It has chiral symmetry and inversion symmetry, and thus exhibits the topological dissipation spectrum for $v < w$ [Fig. 1(b)], which features edge modes at zero dissipation rates in a bulk dissipative gap, absent for trivial dissipation where $v > w$.

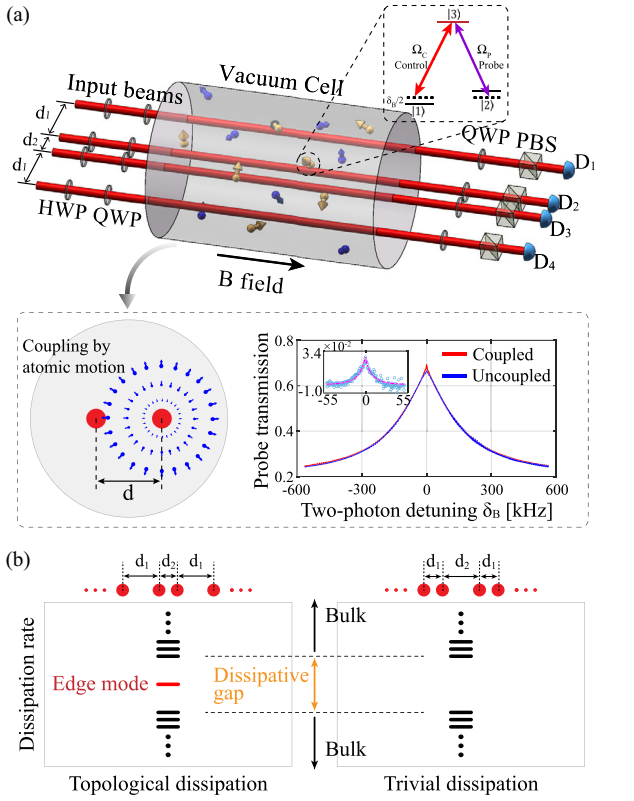

FIG. 1. Schematics and principle of atomic vapor cell experiment simulating SSH model with dissipative couplings. (a) Setup. Top: several optical channels with designed spacings in the vapor cell create ground-state coherences (spin waves) by EIT process in each channel. Spin waves in neighboring channels couple to one another naturally through atomic motion, hence in a dissipative manner, with the coupling rate scaling as $1/d$. An array of spin waves with alternating spacings d_1 and d_2 synthesizes the dissipative SSH model. The output probe intensities are measured to extract properties of the model. Bottom left: coupling mechanism. Bottom right: characterization of dissipative coupling rate using a two-channel setting; the dissipative coupling rate is measured from the difference of EIT spectra (inset) with and without interchannel couplings (see Supplemental Material [33]). The dashed lines in the inset are the fitting (to guide the eye) of the experimental data shown as dots in the inset. (b) Schematic of the topological and trivial dissipation spectra expected from distinct patterns. The topological dissipation spectrum exhibits dissipative edge modes at isolated dissipation rates within a bulk dissipative gap, in contrast to the trivial spectrum. HWP, half wave plate; QWP, quarter wave plate; PBS, polarization beam splitter.

EIT spectroscopy of topological dissipation spectrum.— We first implement a minimal version of the topological dissipative SSH model with $N = 2$ unit cells in a geometry with open ends, using a chain of four laser beams with spacings $d_1 = 6$ and $d_2 = 3$ mm [cf. Fig. 1(a)]. The dissipative coupling rates are measured as $v \approx 2\pi \times 5$ and $w \approx 2\pi \times 11$ kHz [33], with $v/w \approx d_2/d_1 = 1/2$ as expected. The background dephasing rate is measured as $\gamma \approx 2\pi \times 143$ kHz, which is barely affected by the inter-channel couplings because $v, w \ll \gamma$.

We probe the non-Hermitian Hamiltonian H via measuring the probe field's transmissions by sweeping δ_B. Both the frequency and power of the laser are stabilized, and the laser polarization is carefully controlled. For an input $\mathbf{P}_{\text{in}}$, the output probe intensities are determined by the real part of the ground-state coherences,

$$\boldsymbol{\rho}_{12} = -i[(\delta_B - i\gamma)I + H]^{-1}\mathbf{P}_{\text{in}}. \tag{2}$$

Thus, information of H is encoded in the *difference* of $\boldsymbol{\rho}_{12}$ from $\boldsymbol{\rho}^0_{12} = -i(\delta_B - i\gamma)^{-1}\mathbf{P}_{\text{in}}$ in the uncoupled case (i.e., only the probe in the detected channel is on while all control fields are kept on). As the couplings are small and δ_B dependent, this difference is only significant in a narrow spectral window $|\delta_B| \lesssim v, w$ around the EIT center and, therefore, reflects essentially the purely dissipative case described by H_0 (i.e., when $\delta_B = 0$).

We detect the dissipation spectrum of H_0 via eigen-EIT spectroscopy. Let us label the eigendissipation rates of H_0 by γ_σ ($\sigma = 1, \ldots, 4$), which are defined by $H_0\psi_\sigma = i\gamma_\sigma\psi_\sigma$, where ψ_σ denotes the corresponding eigenstates. To measure γ_σ, we harness the flexible control over the input light to design an eigenstate-form input $\mathbf{P}_{\text{in}} \propto \psi_\sigma$, which results in spin waves and hence an eigen-EIT supermode according to $\boldsymbol{\rho}_{12,\sigma} \propto \psi_\sigma/(-i\gamma + i\gamma_\sigma)$. Here, an eigenstate-form input is directly mapped to the spatial distribution of the output probe laser power in each channel. After some algebra, we obtain the relation between the eigen-dissipation rates and the coupled and uncoupled ρ_{12} in all the channels ($j = 1, \ldots 4$),

$$\left.\frac{\rho^{(j)}_{12,\sigma} - \rho^{0,(j)}_{12,\sigma}}{\rho^{0,(j)}_{12,\sigma}}\right|_{\delta_B=0} = \frac{1}{1 - \gamma_\sigma/\gamma} - 1, \tag{3}$$

where $\boldsymbol{\rho}^0_{12,\sigma} \propto \psi_\sigma/(-i\gamma)$. Equation (3) is our central principle to accurately extract the dissipation spectrum.

Experimentally, we probe the four eigen-EIT supermodes in the lattice with $d_1/d_2 \approx 2$ using four input vector states $\mathbf{P}_{\text{in}}$ denoted as $[-7, -3, 3, 7]^T$, $[7, -3, -3, 7]^T$, $[3, 7, 7, 3]^T$, and $[-3, 7, -7, 3]^T$, respectively. These inputs resemble the theoretically predicted eigenstates of H_0 with $v/w = 1/2$: the former (latter) two mimic the edge (bulk) states. Here, numbers "± 7" and "± 3" represent the relative (approximate) values of $\Omega_c^*\Omega_p$ in each channel, "7" ("3") corresponds to a probe power of 9.5 μW (1.7 μW), while all control powers are fixed at 95.5 μW, and the $\pm$ sign is determined by the control and probe's relative phase, which are all judiciously set by tuning the wave plates in the light streams (see Supplemental Material [33]). Since any channel yields the same eigenvalue according to Eq. (3), we choose to measure the transmission spectra of the two channels with relatively higher probe power, thus higher signal-to-noise ratio, to extract an averaged eigenvalue. Figures 2(a1)–2(d1) show the four measured eigen-EIT spectra. We observe that the eigen-EIT spectra corresponding to the edge-state inputs nearly overlap with the uncoupled EIT [Figs. 2(a1)–2(b1)], signaling the "zero" eigendissipation rates (i.e., $\gamma_\sigma \approx 0$). In contrast, the bulk EIT supermodes in Figs. 2(c1)–2(d1) change significantly in both the peak intensity and the linewidth compared to the uncoupled case; an increase (decrease) in the peak intensity indicates dissipation rates $\gamma_\sigma > 0$ or $\gamma_\sigma < 0$ following from Eq. (3). In Figs. 2(a2)–2(d2), we present theoretical calculations [33] using Eq. (1) with measured v

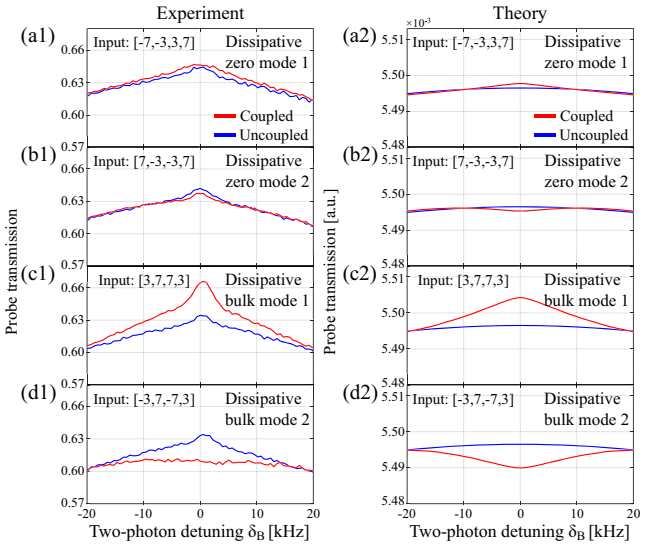

FIG. 2. Detections of the dissipation rates of edge and bulk modes in a topological dissipative SSH chain through eigen-EIT spectroscopy. The chain constitutes four channels in Fig. 1(a) with spacings $d_1 = 6$ and $d_2 = 3$ mm, leading to dissipative coupling rates $v \approx 2\pi \times 5$ and $w \approx 2\pi \times 11$ kHz. Only the center parts of the spectra manifesting influences from the dissipative SSH couplings are shown. (a1)–(d1) Measured eigen-EIT spectra via the probe transmission (normalized to far off resonant 100% transmission), coupled (all channel probes on) and uncoupled (only probe in the detected channel on), for the four input states $[-7, -3, 3, 7]^T$, $[7, -3, -3, 7]^T$, $[3, 7, 7, 3]^T$, $[-3, 7, -7, 3]^T$, respectively. The former (latter) two inputs approximate the two edge (bulk) states of the dissipative SSH model with dissipative coupling rates $v/w = 1/2$. The difference between the coupled and uncoupled peak intensities provides the eigendissipation rates according to Eq. (3). Theoretical calculations of the optical coherences are shown in (a2)–(d2).

and w values. As shown, the relative trends in the coupled and uncoupled EIT spectra shown by the calculation are consistent with that in the experiment data, with the remaining disagreement in that experimental uncoupled EIT spectra are pointier than the theoretical ones, because the theory model gives an idealized Lorentzian line shape that disregards experimental complications [33].

Finally, we obtain the dissipation rates based on Eq. (3), using the measured peak intensities in the coupled and uncoupled cases in Figs. 2(a1)–2(d1). The constructed dissipation spectrum for $v/w \approx 1/2$ is shown in Fig. 3(a). The key feature is the existence of two nearly zero dissipation rates deep within the expected dissipative gap of size $2|v-w| = 2\pi \times 12$ kHz; note the small degeneracy splitting is a natural consequence of the small system size here. By contrast, the other two dissipation rates are in the spectral bulk outside the gap.

To compare the spectra in topologically distinct phases, we swap the channel spacing to realize a configuration with $d_1 = 3$ and $d_2 = 6$ mm, corresponding to $v/w \approx 2$. Using eigen-EIT spectroscopy, we construct the dissipation spectrum [Fig. 3(b)]. All the dissipation rates are now outside the gap, in contrast to the topological spectrum [Fig. 3(a)].

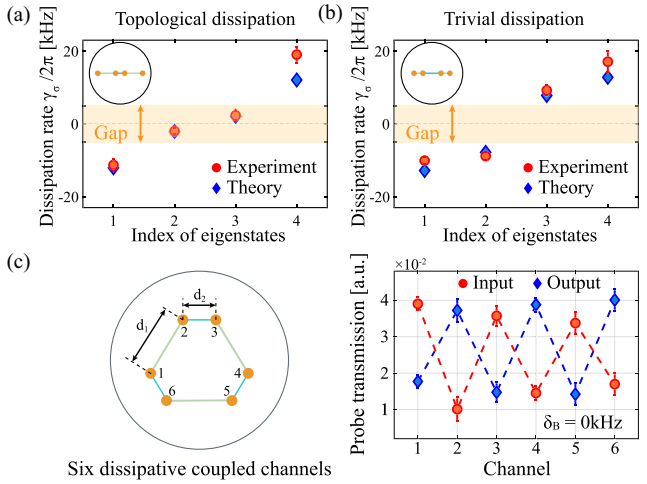

FIG. 3. Observing features of topological dissipation. (a),(b) Dissipation spectra for a dissipative SSH chain in (a) topological and (b) trivial regimes. The dissipation rates γ_σ, $\sigma = 1, \ldots, 4$, are measured via eigen-EIT spectroscopy. The red dots denote the experimental data. The blue dots show predicted values from our theoretical model with (a) $v/w = 1/2$ and (b) $v/w = 2$. The orange region shows the expected dissipative gap. The insets illustrate the cross sections of (a) topological and (b) trivial patterns of four coupled optical channels in the vapor cell. (c) Chiral symmetry. Left: illustrates the cross section of six channels forming a ring with spacings $d_1 = 6$ and $d_2 = 3$ mm. Right: the input probes (red) across the channels simulate $[1,0,1,0,1,0]^T$. The "output" probe laser intensities (blue) are the measured probe output differences between the coupled and uncoupled cases at $\delta_B = 0$. In (a)–(c), the error bar is the standard deviation from about ten repetitive experiments.

For both, the dissipation rates distribute nearly symmetrically around zero. The experiment agrees with the calculations from diagonalizing H_0 with $v/w = 1/2$ and $v/w = 2$, respectively. The discrepancy between the experiment and theory, especially for the largest eigenvalue, is due to the residual returned atomic coherence after wall collisions and other experiment imperfections (see Supplemental Material [33]).

Probe chiral symmetry in a ring.—We next probe potential chiral symmetry of the dissipative SSH model (1). To this end, we construct a ring configuration with six laser beams [Fig. 3(c)] to implement the model with $N = 3$ unit cells under periodic boundary condition. The chiral symmetric operator S of a SSH ring is expressed as $S = I \otimes \sigma_z$, where σ_z is the Pauli matrix. For the ring here, I is a 3×3 unity matrix. To experimentally probe chiral symmetry, we exploit the fact that the S has two eigenvectors $S\phi_\pm = \pm\phi_\pm$, with $\phi_+ = [1,0,1,0,1,0]^T$ and $\phi_- = [0,1,0,1,0,1]^T$ (states written for real space, unnormalized) corresponding to different chirality ($\pm$); if H is chiral symmetric, i.e., $SHS^\dagger = -H$, its action on, say ϕ_+, yields the eigenstate with opposite chirality, $H\phi_+ \propto \phi_-$. In this spirit, we prepare an input $\mathbf{P}_{\text{in}} \propto [1,0,1,0,1,0]^T$ and measure the probe transmission change (due to couplings) in the six channels as the output. Signature of chiral symmetry is observed [Fig. 3(c)]: the input in odd-numbered channels leads to an output dominantly in even-numbered channels. We note that, although the presence of beyond-nearest-neighbor couplings breaks chiral symmetry in the strict sense, given that these coupling rates are smaller than v, w ($\ll \gamma$) in our experiment, we are still able to observe residue signature of chiral symmetry in the transmission.

Generalized dissipative SSH chain with ten channels.—In a ringlike pattern, direct atomic flight between the next-nearest neighbor (NNN) channels may lead to nontrivial NNN coupling and modify the topological properties. To examine its effect, we wire up ten channels as an open-end chain with $d_1 = 6$ and $d_2 = 3$ mm [Fig. 4(a)], i.e., $v/w \approx 1/2$. The effective Hamiltonian including NNN couplings is

$$H' = H + H_{\text{NNN}}, \tag{4}$$

where $H_{\text{NNN}} = it\sum_m(|a,m\rangle\langle a,m+1| + |b,m\rangle\langle b,m+1| + \text{H.c.})$ captures dissipative NNN couplings with rate t for $\delta_B \approx 0$. H' represents the dissipative version of the so-called generalized SSH model [32]. Although H' violates chiral symmetry [34], it retains inversion symmetry. Thus, when $v/w \approx 1/2$, H' is topological for $t/w < 1/2$, which hosts two degenerate edge modes with dissipation rates $\gamma_\sigma < 0$ [33]. Our realized array has $t/w \approx 1/3$ [Fig. 4(a)] and remains in the topological regime, but with a reduced gap $2t \approx 2\pi \times 6.67$ kHz. Note, H' and H share the same eigenstates in the bulk, but the spectrum of H' is

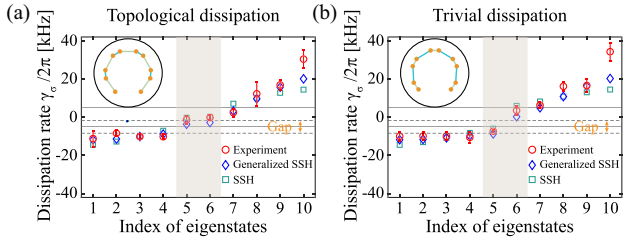

FIG. 4. Implementing the generalized dissipative SSH model with ten channels in (a) topological and (b) trivial regimes. Cross sections of the open-end array are shown in the insets with (a) $d_1 = 6$ and $d_2 = 3$ mm; (b) $d_1 = 3$ and $d_2 = 6$ mm. In the main panels, the red dots denote the experimental data. The blue diamonds denote the theoretical eigenvalues of the generalized dissipative SSH Hamiltonian (4), and regions between the dashed lines indicate the gap. For comparison, the green squares denote the theoretical simulations from the dissipative SSH Hamiltonian H, and the gap is drawn by the solid lines. The vertical shaded area highlights the modes of particular interest (see text). The error bar is the standard deviation from about ten repetitive experiments. The eigenstates (unnormalized) of the two edge modes are $[-0.56, 0.25, 0.24, -0.16, -0.21, 0.21, 0.16, -0.24, -0.25, 0.56]$, $[0.62, -0.17, -0.26, -0.02, 0.14, 0.14, -0.02, -0.26, -0.17, 0.62]$ in terms of ground-state coherence, corresponding to input probe powers of $[8.0, 1.6, 1.5, 0.7, 1.2, 1.2, 0.7, 1.5, 1.6, 8.0]$, $[10, 0.8, 1.7, 0.01, 0.5, 0.5, 0.01, 1.7, 0.8, 10]$ μW, respectively. The control beam powers in all channels are the same, ∼95 μW. Experiment results for the input states corresponding to the largest eigenvalues are affected the most by the couplings beyond the NNN, leading to greater discrepancy between the experiment and theory, because other input states have a more densely interwoven distribution of positive and negative spin coherences, which tends to average out the influences from sites further away. For instance, the first, second, eighth, ninth, and tenth eigenstates (unnormalized) in the topological regimes are, respectively, $[-0.08, 0.26, -0.11, -0.49, 0.41, 0.41, -0.49, -0.11, 0.26, -0.08]$, $[0.07, -0.41, 0.38, 0.18, -0.39, 0.39, -0.18, -0.38, 0.41, -0.07]$, $[-0.31, -0.40, -0.29, 0.20, 0.35, 0.35, 0.20, -0.29, -0.40, -0.31]$, $[0.22, 0.40, 0.43, 0.29, 0.16, -0.16, -0.29, -0.43, -0.40, -0.22]$, $[0.11, 0.25, 0.31, 0.39, 0.42, 0.42, 0.39, 0.31, 0.25, 0.11]$.

shifted by $\Delta\gamma_k = 2t\cos k$ with respect to H in the momentum space [34].

Experimentally, we measure the dissipation spectrum of H' via the eigen-EIT spectroscopy, where the input states are engineered as the eigenstates of H' with $v:w:t \approx \frac{1}{2}:1:\frac{1}{3}$. The experimental data are shown in Fig. 4(a). Furthermore, we swap the channel spacing to realize H' with $v:w:t = 1:\frac{1}{2}:\frac{1}{3}$ in the nontopological regime, and extract its spectrum as shown in Fig. 4(b). Each eigenvalue is the averaged value of that measured from the transmission spectrum of the four channels with relatively higher probe powers. The experimental data are in good agreement with the calculated eigenvalues of H'. Although H' with $t/w \approx 1/3$ is close to the phase boundary, comparison of Figs. 4(a) and 4(b) (especially the shaded regions) still allows us to distinguish the nearly degenerate, surviving edge modes [see Fig. 4(a)] in the topological regime. Moreover, to extract the spectral shift due to NNN couplings, we compare the experiment with the theoretical simulation of the eigen-EIT transmission using Eq. (2) with H instead of H'. We observed the expected shift, e.g., both the maximum and minimum dissipation rates of H', associated with $k = 0$, shift upward. The remaining discrepancy between the experiment and theory is mainly attributed to the couplings beyond the NNN in the open-ring structure (see caption of Fig. 4).

Conclusions and outlook.—We have realized a lattice of atomic spin waves with dissipative SSH couplings in a vapor cell and spectroscopically demonstrated key features of topological dissipation. Though the coupling strength remains small compared to the background loss, we expect to reach a stronger coupling regime by engineering the geometry of a wall-coated cell, the laser beam profiles, and their arrangements to prevent all-to-all coupling but still retain coherence protection by the coating. Other means to control the coupling could be incorporated, e.g., diffractive optical coupling [14] and reservoir engineering [27]. Combining with the controllability over atomic spins by multilevel and nonlinear atom-light interactions in each channel [35], our platform holds unique promise for exploring non-Hermitian topology [19,20,22,36–40] in quantum regimes and designing novel quantum-correlated light sources for quantum information applications.

We are grateful to Wei Yi, Tao Shi, Shuai Chen, Heng Shen, Feng Mei, Changrui Yi, and Ruiheng Jiao for discussions. This work is supported by the Natural Science Foundation of China (NSFC) under Grants No. 12161141018, No. 12027806, No. 61675047, and No. 11874038, and by the National Key Research and Development Program of China under Grant No. 2017YFA0304204 and by Fund for Shanxi "1331 Project".

*huying@sxu.edu.cn
†yxiao@fudan.edu.cn

[1] X. G. Wen, *Quantum Field Theory of Many-Body Systems: From the Origin of Sound to an Origin of Light and Electrons* (Oxford University Press, New York, 2004).
[2] M. Z. Hasan and C. L. Kane, Rev. Mod. Phys. **82**, 3045 (2010).
[3] X. L. Qi and S. C. Zhang, Rev. Mod. Phys. **83**, 1057 (2011).
[4] B. A. Bernevig and T. L. Hughes, *Topological Insulators and Topological Superconductors* (Princeton University Press, Princeton, NJ, 2013).
[5] A. Kitaev, Ann. Phys. (Amsterdam) **303**, 2 (2003).
[6] C. Nayak, S. H. Simon, A. Stern, M. Freedman, and S. Das Sarma, Rev. Mod. Phys. **80**, 1083 (2008).
[7] J. K. Pachos, *Introduction to Topological Quantum Computation* (Cambridge University Press, Cambridge, England, 2012).
[8] P. Peng, W. Cao, C. Shen, W. Qu, J. Wen, L. Jiang, and Y. Xiao, Nat. Phys. **12**, 1139 (2016).

[9] Y. Li, Y. Peng, L. Han, M. Miri, W. Li, M. Xiao, X. Zhu, J. Zhao, A. Alù, S-H. Fan, and C. Qiu, Science **364**, 170 (2019).
[10] Y. Choi, C. Hahn, J. W. Yoon, and S. H. Song, Nat. Commun. **9**, 2182 (2018).
[11] F. Huang, L. Chen, L. Huang, J. Huang, G. Liu, Y. Chen, Y. Luo, and Z. Chen, Phys. Rev. A **104**, L031503 (2021).
[12] A. Bergman, R. Duggan, K. Sharma, M. Tur, A. Zadok, and A. Alù, Nat. Commun. **12**, 486 (2021).
[13] F. Zhang, Y. Feng, X. Chen, L. Ge, and W. Wan, Phys. Rev. Lett. **124**, 053901 (2020).
[14] G. Arwas, S. Gadasi, I. Gershenzon, A. Friesem, N. Davidson, and O. Raz, Sci. Adv. **8**, eabm7454 (2022).
[15] S. Diehl, E. Rico, M. Baranov, and P. Zoller, Nat. Phys. **7**, 971 (2011).
[16] C. Bardyn, M. A. Baranov, C. Kraus, E. Rico, A. Imamoglu, P. Zoller, and S. Diehl, New J. Phys. **15**, 085001 (2013).
[17] A. Metelmann and A. A. Clerk, Phys. Rev. X **5**, 021025 (2015).
[18] K. Fang, J. Luo, A. Metelmann, M. H. Matheny, F. Marquardt, A. A. Clerk, and O. Painter, Nat. Phys. **13**, 465 (2017).
[19] S. Yao and Z. Wang, Phys. Rev. Lett. **121**, 086803 (2018).
[20] F. K. Kunst, E. Edvardsson, J. C. Budich, and E. J. Bergholtz, Phys. Rev. Lett. **121**, 026808 (2018).
[21] C. C. Wanjura, M. Brunelli, and A. Nunnenkamp, Nat. Commun. **11**, 3149 (2020).
[22] E. J. Bergholtz, J. C. Budich, and F. K. Kunst, Rev. Mod. Phys. **93**, 015005 (2021).
[23] C. Leefmans, A. Dutt, J. Williams, L. Yuan, M. Parto, F. Nori, S-H. Fan, and A. Marandi, Nat. Phys. **18**, 442 (2022).
[24] O. Firstenberg, M. Shuker, A. Ron, and N. Davidson, Rev. Mod. Phys. **85**, 941 (2013).
[25] I. Novikova, R. Walsworth, and Y. Xiao, Laser Photonics Rev. **6**, 333 (2012).
[26] W. Cao, X. Lu, X. Meng, J. Sun, H. Shen, and Y. Xiao, Phys. Rev. Lett. **124**, 030401 (2020).
[27] X. Lu, W. Cao, W. Yi, H. Shen, and Y. Xiao, Phys. Rev. Lett. **126**, 223603 (2021).
[28] S. Mittal, E. A. Goldschmidt, and M. Hafezi, Nature (London) **561**, 502 (2018).
[29] A. Blanco-Redondo, B. Bell, D. Oren, B. J. Eggleton, and M. Segev, Science **362**, 568 (2018).
[30] H. Cai, J. Liu, J. Wu, Y. He, S.-Y. Zhu, J.-X. Zhang, and D.-W. Wang, Phys. Rev. Lett. **122**, 023601 (2019).
[31] M. V. Balabas, T. Karaulanov, M. P. Ledbetter, and D. Budker, Phys. Rev. Lett. **105**, 070801 (2010).
[32] L. Li, Z. Xu, and S. Chen, Phys. Rev. B **89**, 085111 (2014).
[33] See Supplemental Material at http://link.aps.org/supplemental/10.1103/PhysRevLett.130.153602 for details of the theoretical models, extended experiment data and descriptions of experiment imperfections.
[34] The Bloch Hamiltonian associated with H' is $2it(\cos k)I + i(v + w\cos k)\sigma_x + iw(\sin k)\sigma_y$ with the unity matrix I, which shares the same eigenstates with the dissipative SSH model. Different from the latter, H' with $v/w = 1/2$ and $t/w = 1/3$ exhibits an indirect gap: The minimum of the upper band and the maximum of the lower band are associated with different momenta.
[35] J. Sun, X. Zhang, W. Qu, E. E. Mikhailov, I. Novikova, H. Shen, and Y. Xiao, Phys. Rev. Lett. **123**, 203604 (2019).
[36] Z. Gong, Y. Ashida, K. Kawabata, K. Takasan, S. Higashikawa, and M. Ueda, Phys. Rev. X **8**, 031079 (2018).
[37] H. Zhou, C. Peng, Y. Yoon, C. Hsu, K. Nelson, L. Fu, J. D. Joannopoulos, M. Soljacic, and B. Zhen, Science **359**, 1009 (2018).
[38] K. Kawabata, K. Shiozaki, M. Ueda, and M. Sato, Phys. Rev. X **9**, 041015 (2019).
[39] L. Xiao, T. Deng, K. Wang, G. Zhu, Z. Wang, W. Yi, and P. Xue, Nat. Phys. **16**, 761 (2020).
[40] Q. Liang, D. Xie, Z. Dong, H. Li, H. Li, B. Gadway, W. Yi, and B. Yan, Phys. Rev. Lett. **129**, 070401 (2022).